A mean field model of agglomeration as an extension to existing precipitation models

Anthony Seret, Charbel Moussa, Marc Bernacki, Nathalie Bozzolo

A mean field model of agglomeration as an extension to existing precipitation models

Anthony Seret*, Charbel Moussa, Marc Bernacki, Nathalie Bozzolo

CEMEF–Centre de mise en forme des matériaux, Mines ParisTech, PSL–Research University
CNRS UMR 7635, CS 10207 rue Claude Daunesse 06904 Sophia Antipolis Cedex France

Abstract

This work presents an analytical mean field model of agglomeration (equivalent agglomeration model, EAM) by contact between growing precipitates. The principle of the EAM is to add a 2-steps task to existing precipitation models: at each time-step, (1) calculate the number of agglomerations per unit volume, then (2) use it to update the numbers and radii of classes in order to take agglomeration into account. The first step is validated by full-field simulations of growing spheres randomly placed in a cube. The EAM can be added as extension to existing precipitation models and be applied to the mean radius, multi-class Lagrangian and multi-class Eulerian representations of the precipitate population. The EAM is incorporated to a mean field precipitation model based on the classical nucleation theory and Zener's law for size evolution, and catches the rarefaction of γ'' precipitates agglomerating as they grow during an isothermal annealing in a nickel-based superalloy.

Keywords: Precipitation, agglomeration, mean-field analysis

Introduction

Precipitates influence materials properties through various mechanisms like precipitation hardening and grain size control. Modeling precipitation kinetics at different length and time scales is then a key topic. Different approaches

*Corresponding author

range from the atomic to the macroscopic length and time scales: atomistic kinetic Monte-Carlo [1, 2, 3, 4], molecular dynamics [5, 6, 7] (including their "coarse" variation [8]), cluster dynamics [4, 9, 10, 11, 12], phase fields [13, 14, 15, 16, 17, 18], classical nucleation [19, 20, 21, 22, 23, 24, 25, 3] and growth [26, 27, 28, 29] theories, used in [30, 31, 32, 33, 34, 35, 36, 37] and reviewed in [38], Johnson-Mehl-Avrami-Kolmogorov equation [39, 40, 41, 42, 43, 44].
This work focuses on mean field methods plebiscited for their reduced computational ressources compared to full field methods. Ignoring the location of each individual precipitate limits the information available to describe their interactions. A particular case of interaction is the contact between growing precipitates whose center is fixed, which constitutes the topic of this work.

In mean field models, different representations exist to describe the precipitates population. Some results in the litterature bring elements of a response to the modeling of agglomeration within these representations. A first representation is the mean radius, where the precipitates population is described by its mean radius and number per unit volume. This approach was initially developped by Langer and Schwartz [45]. Nucleation, growth and coarsening of precipitates was treated as concomitant processes, and a steady-state nucleation theory and a linearized version of the Gibbs–Thomson equation were used. This model was later modified by Kampmann and Wagner [46] to describe precipitation in supersaturated solid solution. To describe a continuous evolution from the growth to the Ostwald's ripening of precipitates, Deschamps and Brechet described the time evolution of the mean radius by a weighting approach between the growth equation and the Ostwald's ripening equation [29]. A second representation considers the full precipitate radius distribution. Its time evolution is governed by a balance equation [30] (hereafter called global equation), involving a source term for the nucleation, a flux term for the size evolution and a sink term for the dissolution. In most cases, the global equation is too complicated to be solved analytically due to the presence of radius and/or time dependent terms. Hence multi-class representations of the precipitate radius distribution have been developped, for which the global equation is solved nu-

merically. In particular, such multi-class representations include the Lagrangian representation [36, 38, 47] and the Eulerian one [31, 38, 47]. Their names and principles come from particle tracking in fluid mechanics. In the Lagrangian representation, classes are defined by physical precipitates which are tracked and followed upon time. Concretely, each class is thus defined at each time by a number, a radius and a chemical composition of precipitates. A class is created to account for the nucleation of precipitates, the radius of each class is updated to account for the size evolution, and a class is deleted to account for the dissolution of its precipitates. Consequently, the mean radius representation is a particular case of the Lagragian representation, where only one class is considered. In the Eulerian representation, each class is defined by a fixed radius interval where precipitates enter and leave over time. Concretely, the number of precipitates in each class evolves over time, based a balance whose control volume is the radius interval. The balance considers precipitates entering the class by nucleation (source) and/or size evolution (flux) and leaving the class by size evolution (flux) and/or dissolution (sink). Class managements of both Lagrangian and Eulerian representations are shown in figure 1a and figure 1b respectively. To take agglomeration into account, Smoluchowski [48] was the first to propose an analytical analysis, and embedded agglomeration in the global equation by adding to it a source/sink term (hereafter called agglomeration term). From the global equation including the agglomeration term, Ratke notably derived the precipitate mean radius and number time evolutions if agglomeration is the only physical mechanism occuring, and he applied it to Pb precipitates in Al–Pb alloys [49]. The mean radius notably follows a cube-root-over-time law, similar to the Liftshit, Slyozov and Wagner law [27, 28] which models Ostwald's ripening [50]. This result was used by Massoumi *et al.* [51] to take concomittant agglomeration and Ostwald ripening of γ' precipitates into account in a nickel-based superalloy, regarding the time evolution of the mean radius and number per unit volume. However, to the knowledge of the authors, no study has yet approached the mean field modeling of simultaneous nucleation, size evolution, dissolution and agglomeration of precipitates by ei-

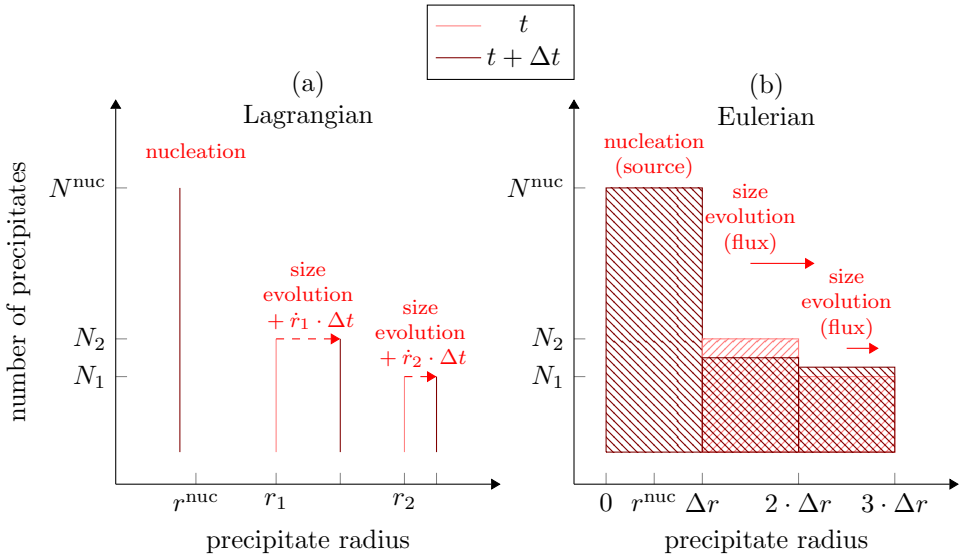

Figure 1: Two possible multi-class representations of the precipitate population by sorting them in classes depending on their radii. (a) Lagrangian approach. Each class is defined by the set of actual precipitates having the same radius. For each class, its radius is updated at each time-step based on the size evolution law. A class is respectively created/deleted when precipitates nucleate/dissolve. (b) Eulerian approach. Each class is defined by a constant radius interval and hosts different precipitates upon time. For each class, the number of precipitates is updated at each time-step based on a balance involving a flux (size evolution), a source (nucleation) and a sink (dissolution) term.

ther the mean radius or one of both multi-class representations. This lack may be due to two difficulties. The first difficulty is to quantify the occurence of agglomeration. More concretely, this consists in assessing the number of agglomerations between precipitates. The second difficulty is to incorporate this quantification into the representation of the precipitate population. More concretely, in the mean radius representation, the effect of agglomeration must be traduced in terms of mean radius and number of precipitates per unit volume; in the multi-class representations, the effect of agglomeration must be traduced in terms of class management. To address this problem, this work proposes a model called equivalent agglomeration model (EAM) which answers by design both previously described difficulties. Indeed, the principle of the EAM is to add a two-steps task at the end of each time-step of any existing model which deals with nucleation, size evolution and dissolution but not agglomeration. The first step is to quantify the occurence of agglomeration by calculating the number of agglomerations per unit volume during the time-step, based on topological and probability calculations. Then, the second step is to incorporate this quantification into the representation of the precipitates population by updating the radii and numbers of precipitates accordingly. The fact that this two-steps task is applied at the end of each time-step of existing models implies that the EAM can be added as an extension to an already implemented model. Section 1 presents the overall precipitation model used, including the EAM in section 1.3. In particular, section 1.3 details the two steps of the EAM: (1) the calculation of the number of agglomerations per unit volume during a time-step, and (2) the update of radii and numbers of precipitates depending on the representation. Then section 2 presents an application case on the precipitation and agglomeration of γ'' precipitates in Inconel 625 nickel-based superalloy during isothermal annealing.

1. Precipitation model

In this section the precipitation model is presented, made of three consecutive parts. The first part is dedicated to the modeling of the physics of nu-

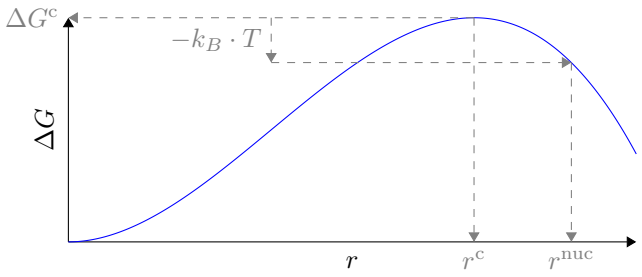

Figure 2: Free enthalpy change ΔG induced by forming a spherical precipitate as a function of its radius r. Critical radius r^{c}, nucleation radius r^{nuc} and free enthalpy barrier ΔG^{c}.

cleation, size evolution and dissolution of precipitates. The classical nucleation theory [19, 20, 21, 22, 23, 24, 25, 3] is used for nucleation and the Zener's law for size evolution [26] is used for size evolution. The second part focuses on the description of the precipitate population using the Lagrangian multi-class representation [36, 38, 47]. The third part presents the core novelty of this work, that is the equivalent agglomeration model (EAM) dedicated to agglomeration by contact beetween growing precipitates.

1.1. Modeling of the physics of nucleation, size evolution and dissolution

1.1.1. Nucleation

The nucleation radius r^{nuc} and the number of precipitates nucleating per unit volume of matrix and per time unit (hereafter abbreviated volumic nucleation rate) are calculated from the classical nucleation theory, as used by Den Ouden [32]. Figure 2 illustrates the typical representative curve of the free enthalpy change (resulting from chemical, elastic and interface contributions) when inserting a spherical precipitate in the matrix as a function of its radius, which defines the free enthalpy barrier ΔG^{c} and the nucleation radius r^{nuc}. The fact that precipitates contain several chemical elements in the application case hereafter (section 2) imposes care regarding the calculation of the segregation rate. Indeed, the precipitation model will be applied to γ'' precipitates defined as a Ni_3X DO_{22} body-centered tetragonal phase [52, 53, 54] where X can be niobium [53, 54], tantalum [52, 55], aluminium [54] or titanium [54]. The material used here is the nickel-based superalloy Inconel 625 [56] in which γ''

precipitates have been reported to precipitate [54, 57, 58, 59, 60, 61] after a typical thermal annealing of 500 hours at 650 °C [61]. In Inconel 625, niobium seems to be the main chemical element taking the role of the X atom [54], then it is considered that X is only niobium and thus γ'' precipitates are Ni_3Nb. Nickel atoms are immediately available in the matrix crystal and thus do not kinetically limit the segregation. Hence the calculation of the segregation rate only considers niobium and consequently reverts to the case of the monoatomic precipitate. Nucleation is calibrated by applying a multiplicative factor $\mathtt{p}_\mathtt{r}^\mathtt{nuc}$ to r^{nuc} and an additive term $-\mathtt{\Delta G}$ to ΔG^{c}. Regarding the first calibration parameter, concretely the classical nucleation theory predicts that for the current time-step the nucleation radius is r^{nuc}: in the model the class representing newly nucleated precipitates is then created with a radius $\mathtt{p}_\mathtt{r}^\mathtt{nuc} \cdot r^{\mathrm{nuc}}$. Thus the calibration parameter $\mathtt{p}_\mathtt{r}^\mathtt{nuc}$ allows to adjust the radius at which precipitates nucleate, which can influence the kinetics of size evolution. Regarding the second calibration parameter, concretely the classical nucleation theory predicts that for the current time-step, the critical free enthalpy barrier is ΔG^{c}: in the model the critical free enthalpy change considered is $\Delta G^{\mathrm{c}} - \mathtt{\Delta G}$. The calibration parameter $\mathtt{\Delta G}$ enables to adjust the critical free enthalpy barrier for nucleation and thus helps to control the nucleation rate. If $\mathtt{\Delta G}$ is positive/negative, nucleation is favored/hindered respectively.

1.1.2. Size evolution

The time derivative of the radius of a precipitate is calculated following the Zener's law [26] within the approximation of a low supersaturation. This calculation asserts that the size evolution of precipitates is kinetically limited by the solute diffusion in the matrix towards precipitates, and not by the crossing of the matrix–precipitate interface. This is considered to be true based on th work of Devaux *et al.* work [62] who concluded that the coarsening of γ'' precipitates in Inconel 718 was kinetically limited by the niobium diffusion in the matrix towards the precipitates. However, the fact that precipitates contain several chemical elements in the application case hereafter (Ni_3Nb) imposes care

regarding two points. The first point is the Gibbs[63, 64]-Thompson[65, 66, 67] effect, treated here as proposed by Perez [68]. The second point is the calculation of the radius time derivative, which involves all the atoms present in the precipitate phase (nickel and niobium). However, like for the calculation of the segregation rate, nickel atoms are immediately available in the matrix crystal and thus do not kinetically limit the size evolution. Hence the calculation of the radius time derivative only considers niobium and consequently reverts to the case of the monoatomic precipitate. Size evolution is calibrated by applying a multiplicative factor $\mathtt{p}_{\mathtt{r}}^{\mathtt{se}}$ to the time derivative of the radius. Such a calibration parameter can take into account the fact that some assumptions are not perfectly satisfied. For example, actual precipitates are not spherical and/or actual diffusion-governed profiles of solute concentration profiles can overlap between precipitates.

1.1.3. Dissolution

Two cases can imply the dissolution (defined here as the complete disappearance of a precipitate). The first case occurs if the radius of a precipitate is small enough that the calculation of the Gibbs-Thompson effect leads to a niobium concentration higher in the matrix at the matrix/precipitate interface than in the precipitate. In such case, the precipitate is considered as shrinking infinitely fast *i.e.* dissolved and is immediately deleted. The second case occurs if the radius of a precipitate is below a minimal radius. This minimal radius is the one of a ball with same volume as the unit cell of the precipitate crystal. The precipitate is then considered as dissolved and is immediately deleted.

1.2. Representation of the precipitate population

The precipitate population is modelled by a multi-class representation. Contrary to the mean radius approach, this allows for the description of multimodal size distributions. Such case can appear for example in γ/γ' nickel-based superalloys where γ' precipitates nucleate through several bursts upon a slow enough cooling [69, 70, 51, 71, 72, 73, 74, 75]. In this work, the Lagangian multi-class

representation is used. It presents the three following advantages over the Eulerian multi-class representation. First, the Lagrangian multi-class representation does not require to define classes of fixed radii intervals prior to the simulation, which avoids any influence of such a choice on the results. Second, no majoration on the time-step is needed, whereas classes of fixed radii intervals impose such a majoration to prevent a precipitate from crossing an entire class [38, 47]. Third, in the Lagrangian appproach precipitates with different chemical compositions can readily be considered, whereas in the Eulerian approach this seems to be less straightforward [36, 38, 47].

1.3. Equivalent agglomeration model

The third part of the precipitation model is the equivalent agglomeration model (EAM), the core novelty of this work.

The principle of the EAM consists in applying at the end of each time-step a separate and additional two-steps task after the (already performed) computation of class evolution (due to nucleation, size evolution and dissolution). Consequently, the EAM can be added as an extension to any existing precipitation model, by adding this two-steps task at the end of each time-step. Figure 3 illustrates the procedure of the EAM during one time-step.

1.3.1. Calculation of the number of agglomerations per unit volume

The first step is to calculate $\mathcal{N}_V^{\text{agg}}$ the number of agglomerations per unit volume during a time-step by contacts between growing precipitates.
Consider a population of spherical precipitates placed randomly without intersecting at the beginning of a time-step. To calculate $\mathcal{N}_V^{\text{agg}}$, it is asserted that the phenomena controlling precipitate evolution proceed in two successive mechanisms: (1) size evolution of the precipitates already present at the beginning of the time-step (possibly with dissolution *i.e.* disapperance of some of them) possibly with agglomeration then (2) nucleation of new precipitates. This two-steps decomposition allows to calculate $\mathcal{N}_V^{\text{agg}}$ (associated to the first step) without interference from nucleating precipitates (associated to the second step). It is also assumed that an agglomeration involves exactly two precipitates. Consider the

precipitates already present at the beginning of the time-step, thus undergoing size evolution during the time-step. Their number per unit volume is denoted as $N_{V\text{next}}^{\text{se,no agg}}$, their mean radius as $\overline{r}$, the mean of the time derivative of radii as $\overline{\dot{r}}$ (thus representing the size evolution), its positive part as $\overline{\dot{r}}_+$ (defined by $\overline{\dot{r}}_+ = \max\left\{\overline{\dot{r}}, 0\right\}$) and Δt as the time-step. The calculation of $\mathcal{N}_V^{\text{agg}}$ is based on the calculation of probabilities of encounters of growing precipitates by using their center-to-center distances. The derivation is detailed in Appendix A and yields:

$$\mathcal{N}_V^{\text{agg}} = \frac{1}{2} \cdot N_V \cdot \left(1 - \exp\left(-\mathcal{N}_*^{\text{agg}}\right)\right), \tag{1}$$

where

$$\mathcal{N}_*^{\text{agg}} = \frac{4}{3} \cdot \pi \cdot N_V \cdot \left(\left(2 \cdot \left(\overline{r} + \overline{\dot{r}}_+ \cdot \Delta t\right)\right)^3 - \left(2 \cdot \overline{r}\right)^3\right). \tag{2}$$

The previous calculation was validated by comparing its results with full field simulations of growing spheres placed randomly in a cube, as detailed in Appendix B. The EAM considers simplifying assertions: notably spherical precipitates of the same radius $\overline{r}$ and radius time derivative $\overline{\dot{r}}$). To model agglomeration involving precipitates with different morphology and/or morphological orientation, highly scattered radius and/or radius time derivative distributions, a calibration parameter $\mathtt{p_{agg}}$ is introduced to adjust the number of agglomerations per unit volume during the time-step. Then equation 1 is replaced by:

$$\mathcal{N}_V^{\text{agg}} = \min\left\{\mathtt{p_{agg}} \cdot \frac{1}{2} \cdot N_V \cdot \left(1 - \exp\left(-\mathcal{N}_*^{\text{agg}}\right)\right), \frac{1}{2} \cdot N_V\right\}. \tag{3}$$

The minimum ensures that $\mathcal{N}_V^{\text{agg}}$ is lower than $\frac{1}{2} \cdot N_V$ its maximum physically possible value.

1.3.2. Class update

The second step is to update the (already computed) classes *at the end of the time-step* (grouped into the population $\mathcal{P}$ in figure 3) to take into account agglomeration.

First, the class possibly created during the time-step to model the nucleation is kept unchanged. This corresponds to the assumption that the new precipitates

nucleated at the end of time-step, after the size evolution of the ones already present at its beginning. All other classes (hereafter called *size evolving classes*) then represent precipitates already present at the beginning of the time-step, thus undergoing size evolution during the time-step (hereafter called *size evolving precipitates*). Second, the number and radius of each size evolving class is updated to traduce the overall rarefaction and coarsening of precipitates induced by agglomerations during the time-step. Concretely, the numbers of precipitates belonging to size evolving classes are multiplied by a common factor (α defined hereafter in equation 5) symbolizing their rarefaction; simultaneously, their radii are multiplied by $\alpha^{-\frac{1}{3}}$ to keep the precipitate volume unchanged. The factor α is then the key of the class update and is defined as follows. Consider $N_{V\text{next}}^{\text{se,no agg}}$ the number of size evolving precipitates at the end of the time-step per unit volume, without taking agglomeration into account[1]. Then imagine $N_{V\text{next}}^{\text{se}}$ the number of size evolving precipitates at the end of the time-step per unit volume, now taking agglomeration into account. One the one hand, the number of agglomerations during the time-step per unit volume equals $\mathcal{N}_V^{\text{agg}}$, on the other hand, agglomeration consumes two precipitates to create one. Consequently, this yields:

$$N_{V\text{next}}^{\text{se}} = N_{V\text{next}}^{\text{se,no agg}} - \underbrace{2 \cdot \mathcal{N}_V^{\text{agg}}}_{\text{consumed by agglomeration}} + \underbrace{\mathcal{N}_V^{\text{agg}}}_{\text{created by agglomeration}} . \quad (4)$$

Now the numbers of size evolving precipitates per unit volume, both not taking ($N_{V\text{next}}^{\text{se,no agg}}$) and taking ($N_{V\text{next}}^{\text{se}}$) agglomeration into account are known. Then the factor α is defined as:

$$\alpha = \frac{N_{V\text{next}}^{\text{se}}}{N_{V\text{next}}^{\text{se,no agg}}}. \quad (5)$$

Eventually, all size evolving classes are considered: their precipitate numbers are multiplied by α and simultaneously their radii are multiplied by $\alpha^{-\frac{1}{3}}$ to keep the precipitate volume unchanged. These updated classes then obtained represent size evolving precipitates at the end of the time-step when considering

[1] then $N_{V\text{next}}^{\text{se,no agg}}$ is the sum of the precipitates numbers of all size evolving classes, divided by the material volume (matrix $\cup$ precipitates)

chemical element	Ni	Cr	Nb	Fe	Mo	Mn	Al	Co	C	Ti
mass fraction [%]	base	21.19	3.599	3.88	8.64	0.27	0.2	0.13	0.03	0.25

Table 1: Composition of the used Inconel 625.

the agglomeration. The representation of the precipitate population plays a role here. If the Eulerian multi-class representation is used, then a supplementary task (hereafter called reassignation) must be performed. In this representation, classes are defined by fixed (for the whole simulation) radii intervals. Thus each updated size evolving number-radius pair must be reassigned to appropriate fixed radius interval. Concretely, for each updated radii, the fixed radius interval to which it belongs is located, and the associated number of precipitate is then counted in *i.e.* reassigned to this fixed radius interval. If the Lagragian multi-class or mean radius representation is used, classes are free to have any radius so the reassignation is not necessary.
Combining these updated size evolving classes to the possibly added class modeling nucleation (put aside at the beginning of the class update process) provides a new population. This population represents the precipitates at the end of time-step when taking agglomeration into account. It is then kept as the precipitate population at the end of this time-step ($\mathcal{P}_{\text{next}}$ in figure 3).

2. Application to γ'' precipitates in Inconel 625

2.1. Experimental details

The as-received material is an Inconel 625 sheet homogenized for 4 h at a 1038 °C temperature, supplied by the Safran Nacelles company and whose composition is detailed in table 1. Samples have been annealed under air in a Carbolite furnace then air cooled as presented in figure 4. Evolution of the precipitates upon cooling has been neglected.

Precipitates have been quantitatively characterized as follows. Samples have been mechanically polished Presi abrasive SiC paper #600 to #4000 (5 µm grain size), then electropolished on a LectroPol-5 machine under 45 V tension and 10 A current for 4 s with an (90 % methanol + 10 % perchloric acid) electrolyte bath.

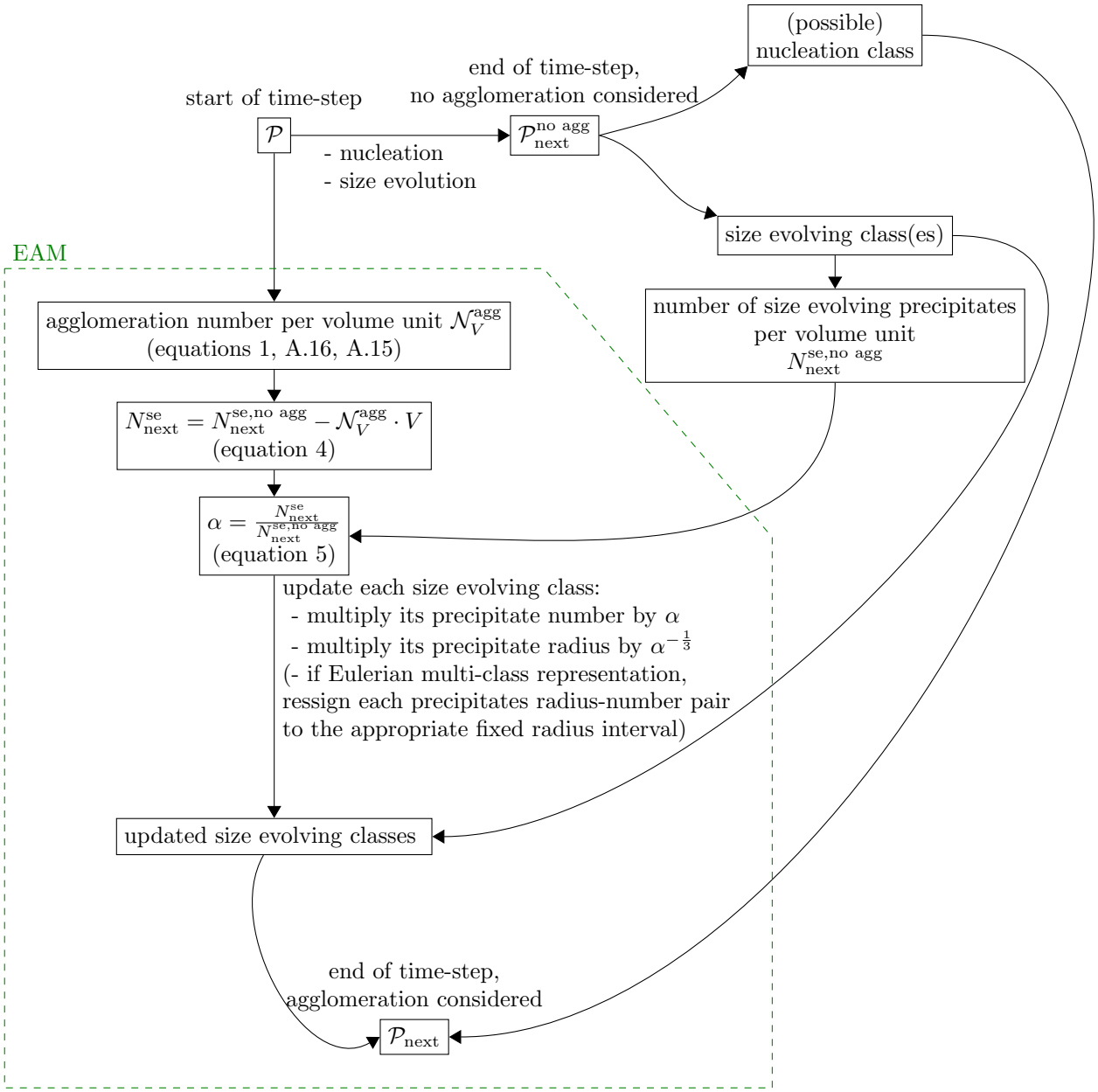

Figure 3: Main steps of the equivalent agglomeration model (EAM) during one-time step.

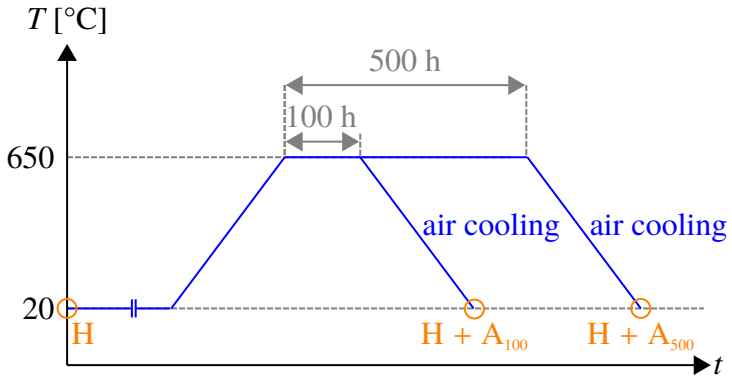

Figure 4: Thermal treatments to trigger the γ'' precipitation. Material states as-received *i.e.* homogenized (H) then annealed at 650 °C for 100 h ($H + A_{100}$) and 500 h ($H + A_{500}$).

The electropolishing etches only the precipitates. The topology then created allowed to observe the location of precipitates (before their etching) on images of plane sections of the material, like those shown in figure 5. To that, a Carl Zeiss Supra 40 scanning electron microscope piloted by the Carl Zeiss SmartSEM sotware was used. The accelerating voltage was 15 kV, the aperture diameter 30 µm, the "high current" option doubling the current was disabled, the acquisition time per image was 3 min 24 s and the detector was an in-lens secondary electron detector. Images have been acquired with the magnification of the ones in figure 5. For each material state, at least 8 images have been considered for analysis, covering an area of at least 8.1 μm^2.

The number of observed precipitates was 6964 and 3212 in the material states $H + A_{100}$ and $H + A_{500}$ respectively. To describe the precipitate size, the two-dimensional/three-dimensional equivalent diameter is defined as the diameter of the disk/sphere with identical area/volume to the one of the precipitate, respectively. The analysis of images thus provides number distributions of two-dimensional equivalent diameter, normalized per area unit of analyzed surface. However, the model represents precipitates as spheres. Thus, to compare precipitates populations assessed experimentally and predicted by the model, number distributions of two-dimensional equivalent diameter, normalized per area unit of analyzed surface, have been converted to number distributions of three-

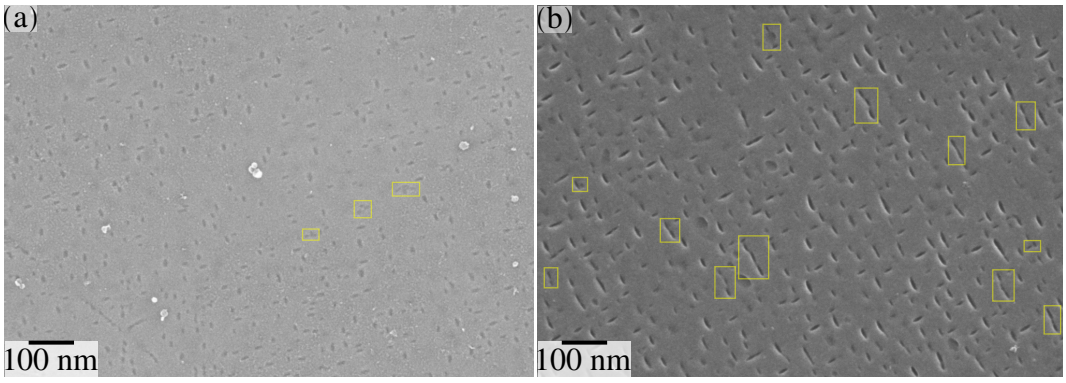

Figure 5: Agglomerating or about-to-agglomerate γ'' precipitates (yellow rectangles) in material states (a) $\mathrm{H} + \mathrm{A}_{100}$ and (b) $\mathrm{H} + \mathrm{A}_{500}$.

dimensional equivalent diameter, normalized per unit volume of material. To that, Saltykov's method [76] was applied by considering the bin width calculated from Scott's method [77]. Hereafter, the expression "equivalent diameter" refers to the three-dimensional one. Number distributions of equivalent diameter, normalized per unit volume of material, are represented as histograms whose bin size is again chosen following Scott's method [77]. Agglomerating precipitates have been observed as shown in figure 5. Precipitates are ellipsoidal (as in [78, 61, 79]) and morphologically oriented according to three variants (as in [58]) in the material state $\mathrm{H}+\mathrm{A}_{500}$, which appears to geometrically favor contact and thus agglomeration (figure 5b).

2.2. Numerical values of physical quantities, calibration parameters, time-step management and computing details

Numerical values of physical quantities have been taken from the litterature and are shown in table 2. In the precipitation model, the values of the calibration parameters $\mathtt{p}_{\mathtt{r}}^{\mathtt{nuc}}$, $\Delta\mathtt{G}$, $\mathtt{p}_{\mathtt{r}}^{\mathtt{se}}$ and $\mathtt{p}_{\mathtt{agg}}$ are indicated in equations 6 to 9 and have been set after less than 40 manual consecutive attempts and modifications. More elaborated optimization methods [82] may allow to reduce the number of calibration parameters needed, for example by removing $\mathtt{p}_{\mathtt{r}}^{\mathtt{nuc}}$. This constitutes

physical quantity	numerical value	reference
lattice constant of matrix conventional unit cell	$3.6073\,\text{Å}$	[80]
lattice constant "a" of precipitate conventional unit cell	$3.6154\,\text{Å}$	[80]
lattice constant "c" of precipitate conventional unit cell	$7.6699\,\text{Å}$	[80]
Young's modulus of matrix	$224\,\text{MPa}$	[81]
Young's modulus of precipitate	$86.5\,\text{MPa}$	[81]
Poisson's coefficient of matrix	$211\,\text{MPa}$	[81]
Poisson's coefficient of precipitate	$79.7\,\text{MPa}$	[81]
Prefactor in Arrhenius law of niobium diffusivity in matrix	$8.8 \times 10^{-6}\,\text{m}^2\,\text{s}^{-1}$	[62]
activation energy of niobium diffusivity in matrix	$4.5167 \times 10^{-19}\,\text{J}$	[62]
energy per unit area of matrix–precipitate interface	$95\,\text{mJ}\,\text{m}^{-2}$	[62]

Table 2: Numerical values of the physical quantities used in the precipitation model.

a perspective for the overall precipitation model.

$$\mathtt{p}_\mathtt{r}^\mathtt{nuc} = 0.8, \tag{6}$$

$$\Delta\mathtt{G} = 2.9 \times 10^{-18}\,\text{J}, \tag{7}$$

$$\mathtt{p}_\mathtt{r}^\mathtt{se} = 0.001, \tag{8}$$

$$\mathtt{p}_\mathtt{agg} = 5. \tag{9}$$

The time-step management is designed to guarantee that, in absolute value, the precipitate volume change during each time-step is always lower than $\frac{1}{100}$ of the precipitate volume change needed to reach the chemical equilibrium *i.e.* equilibrium precipitate volume fraction. Simulations have been performed on a computer equipped with a Intel© Xeon E5-1650 v3 CPU and 24 Go RAM and lasted less than 3 min.

2.3. Results and discussion

Number density distributions of the equivalent diameter of precipitates normalized per unit volume of material (hereafter abbreviated distributions) are presented in figure 6. For a more global information, the number per unit volume, mean equivalent diameter and volume fraction of precipitates are presented over time in figure 7. In both figures, results are presented with both the EAM enabled (equation 9, $\mathtt{p}_\mathtt{agg} = 5$) and disabled ($\mathtt{p}_\mathtt{agg} = 0$) to assess its effects. The model captures in a satisfactory manner experimental distributions

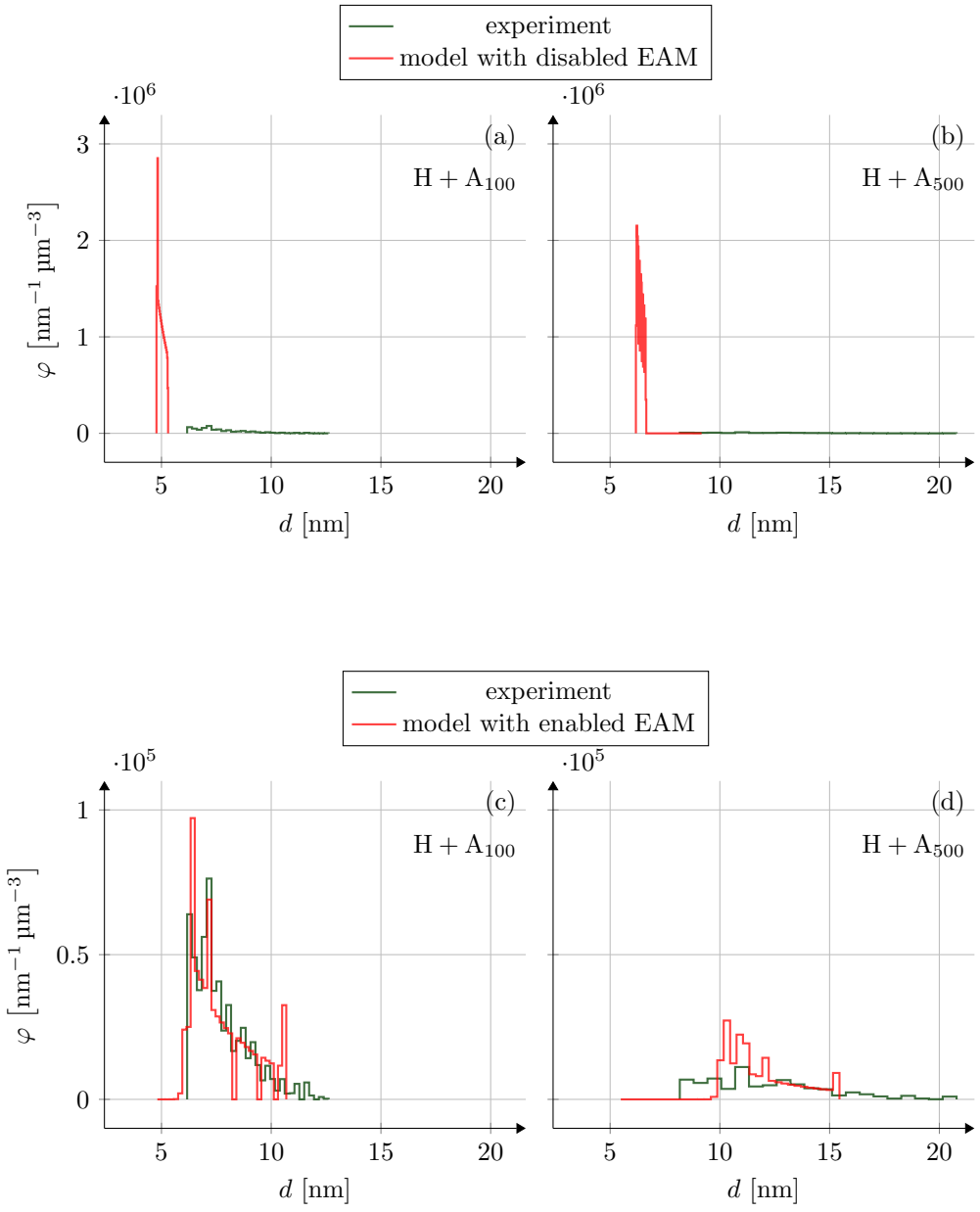

Figure 6: Number density distributions (φ) of the equivalent diameter (d) of the γ'' precipitates, normalized per unit volume of material, experimental (green) and calculated by the model (red) after (a,c) 100 h ($H + A_{100}$) and (b,d) 500 h ($H + A_{500}$) at 650 °C when enabling (a,b) ($p_{agg} = 5$) and disabling (c,d) ($p_{agg} = 0$) the EAM.

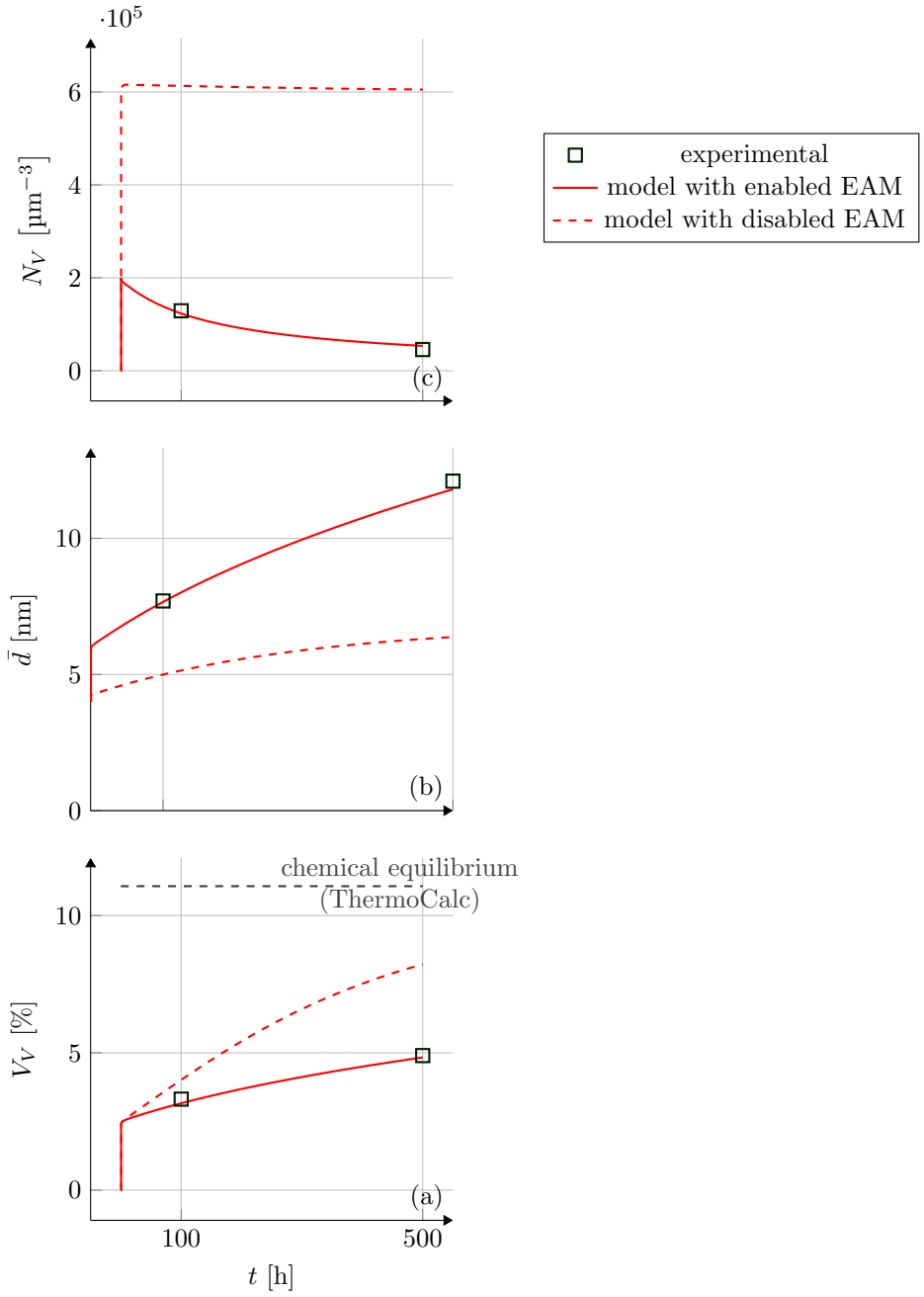

Figure 7: (a) number (N_V) per unit volume, (b) mean equivalent diameter ($\bar{d}$) and (c) Volume fraction (V_V) of precipitates over time, experimental (squares) and calculated by the model (lines). Continuous and dashed lines correspond to the enabled and disabled equivalent agglomeration model (EAM), respectively.

(figure 6) and key quantities (figure 7) when the EAM is enabled (figure 6(c,d)). Regarding the distributions, if the EAM is disabled (figure 6(a,b)), the radii decrease (as expected), and the distribution becomes narrower. This imposes to dilate the ordinate scale to see its maximum value, such that in turn the experimental distribution cannot be seen anymore. Thus the EAM not only induce an increase of radii but also a broadening of the radius distribution. However, it is hard to explain directly this broadening effect. Indeed, in the EAM a multiplying factor (in terms of radius) *common to all classes* is applied at each time-step to these classes. So it is not obvious to understand *differences between classes* in terms of size evolution kinetics. Regarding key quantities (figure 7), enabling the EAM induces an overall rarefaction (figure 7a) and coarsening (figure 7b) of the precipitates over time. Capturing the rarefaction of precipitates was impossible without taking into acount agglomeration. Another result is the fact that when enabling the EAM, the volume fraction (figure 7c) of precipitates increases more slowly over time. This can be explained by that fact that agglomeration produces coarser precipitates which thus grow more slowly based on the Zener's law for size evolution. Regarding the calibration of the precipitation model, three discussion points arise. The first point concerns the parameter `ΔG` adjusting the free enthalpy barrier (thus the volumic nucleation rate) set to 2.9×10^{-18} J (equation 7) thus positive to promote nucleation. This can be explained by the fact that the classical nucleation theory considers homogeneous nucleation whereas actual precipitates nucleate on preferential sites where the free enthalpy barrier is lower. Here, such sites may be dislocations having survived the homogeneization, and promoting nucleation by elastic relaxation when nucleating in their stress/strain field. Elastic relaxation as been proven by analytical calculation [58] to be an explanation for preferential nucleation of γ'' precipitates observed on dislocations in Inconel 625 [58, 60, 79]. This mechanism has also been concluded to take place in other systems like γ' precipitates in AD730TM nickel-based superalloy [83, 84] and gold in alpha iron [85]. Other analytical calculations [86] also support its occurence in the case of an incoherent matrix–precipitate interface. The second point concerns

the parameter $\mathtt{p}_{\mathtt{r}}^{\mathtt{se}}$ adjusting the size evolution set to 0.001 (equation 8) to slow down the kinetics of size evolution. This can be explained by four reasons, which furthermore are combinable. The first reason is that precipitates grow mostly orthogonally to their thickness (as shown by their ellipsoidal morphology), whereas in the used law for size evolution precipitates are considered to grow spherically. Then precipitates probably present a reduced surface for solute atoms coming to feed their growth[2] and thus slower kinetics of size evolution, compared to that expected from the used law of size evolution law. The second reason is that this actual portion of the matrix–precipitate interface welcoming atoms is more curved than if precipitates were spherical. The Gibbs-Thompson effect is then locally more pronounced on this surface, the solute concentration in the matrix at the matrix–precipitate interface near this surface is thus higher than that in the used law for size evolution. Hence the concentration profiles are flatter, the magnitude of concentration gradients are lower and the kinetics of diffusion and size evolution are slower than in the size evolution law used. The third reason related to the diffusivity of solute in the matrix taken from the litterature [62] as that of niobium diffusing in pure nickel. However, the matrix contains other chemical elements in solid solution possibly hindering the diffusion of niobium atoms. In turn, the kinetics of diffusion and size evolution could be slower than that arising from the size evolution used. The fourth reason is that precipitates are relatively close, whereas the law used for size evolution used considers one precipitate in an infinite matrix. This precipitate closeness can flatten the concentration profiles, then reduce the magnitudes of concentration gradients, and thus slow down the diffusion and size evolution. Eventually, the third point concerns the parameter $\mathtt{p}_{\mathtt{agg}}$ adjusting the agglomeration set to 5 (equation 9) to hasten the kinetics of agglomerations. This can be explained by the fact that precipitate are ellipsoidal (as in [78, 61, 79]) and morphologi-

[2] At equal volume, a sphere and a revolution cylinder with aspect ratio of 4 (from figure 5b) present a ratio of $\left(\frac{1}{3}\right)^{\frac{2}{3}} = 0.48$ in terms of surface welcoming niobium atoms (lateral curved surface for the revolution cylinder, full sphere for the ball), explaining partially but insufficently the 0.001 calibration parameter $\mathtt{p}_{\mathtt{r}}^{\mathtt{se}}$.

cally oriented according to three variants (as in [58]) which geometrically favors contacts and thus agglomerations, compared to the spherical shape asserted in the EAM model (see figure A.8).

Conclusion and perspectives

An analytical mean field model (called equivalent aglomeration model, EAM) describing agglomeration by contact between growing precipitates has been presented. The EAM can be added as an extension to existing precipitation models and be applied to the mean radius, multi-class Lagrangian and multi-class Eulerian representations of the precipitate population. The EAM has been applied to the γ'' precipitation during an isothermal annealing of a nickel-based superalloy. In particular, it captures the rarefaction of precipitates upon time due to their agglomerations as they grow and meet, which was otherwise impossible. The EAM also describes in a satisfactory manner the evolution upon time of the size distribution of precipitates.

Two perspectives arise to enhance the EAM. The first perspective is to consider non-spherical and/or non-randomly morphologically oriented precipitates to take into account how this may influence the frequencies of contact and thus agglomeration, as illustrated by the experimental case considered in this work. The second perspective is to use the size distribution of precipitates rather than only their mean radius. This may prove relevant for multimodal precipitate populations, like the γ' precipitates nucleated through several bursts during a slow enough cooling in γ/γ' nickel based superalloys.

Acknowledgement

This work has been carried out within the frame of the OPALE industrial chair co-funded by Safran and the French National Agency for Research ANR. Gilbert Fiorucci, Cyrille Colin and Suzanne Jacomet are acknowledged for their help in performing thermal treatments, sample preparation and scanning electron microscopy analyses, respectively.

References

[1] N. Metropolis, A. Rosemblum, M. Rosenbluth, A. Teller, E. Teller, Equations of State Calculations by Fast Computing Machines, Journal of Chemical Physics 21 (1953) 1087–1092.

[2] J. Lépinoux, C. Sigli, Precipitate growth in concentrated binary alloys: a comparison between kinetic Monte Carlo simulations, cluster dynamics and the classical theory, Philosophical Magazine 93 (23) (2013) 3194–3215.

[3] P. Maugis, F. Soisson, L. Lae, Kinetics of precipitation: comparison between Monte Carlo simulations, cluster dynamics and the classical theories, Defect and diffusion Forum 237–240 (2005) 671–676.

[4] A. Perini, G. Jacucci, G. Martin, Cluster free energy in the simple cubic ising model, Physical Review 29 (1984) 2689–2697.

[5] B. Alder, T. Wainwright, Studies in Molecular Dynamics. I. General Method, The Journal of Chemical Physics 31 (1959) 459–466.

[6] C. Becquart, M. Perez, Dynamique moléculaire appliquée aux matériaux, `http://michel.perez.net.free.fr/Becquart10.pdf` (2010).

[7] F. Zirkelbach, J. Lindner, K. Nordlund, B. Stritzker, Molecular dynamics simulation of defect formation and precipitation in heavily carbon doped silicon, Materials Science and Engineering: B 159-160 (2009) 149–152, eMRS 2008 Spring Conference Symposium K: Advanced Silicon Materials Research for Electronic and Photovoltaic Applications. doi:https://doi.org/10.1016/j.mseb.2008.10.010.

[8] I. Volgin, S. Larin, A. Lyulin, S. Lyulin, Coarse-grained molecular-dynamics simulations of nanoparticle diffusion in polymer nanocomposites, Polymer 145 (2018) 80–87.

[9] L. Laé, Etude de la précipitation en dynamique d'amas dans les alliages d'aluminium et dans les aciers, Ph.D. thesis, Institut national polytechnique de Grenoble (2007).

[10] K. Kelton, A. Greer, C. Thompson, Transient nucleation in condensed systems, Journal of Chemical Physics 79 (1983) 6261–6276.

[11] F. Christien, A. Barbu, Modeling of copper precipitation in iron during thermal aging and irradiation, Journal of Nuclear Materials 324 (2004) 90–96.

[12] E. Clouet, Modeling of nucleation processes, in: D. Furrer, S. Semiatin (Eds.), ASM Handbook, Fundamentals of Modeling for Metals Processing, Vol. 22 of A, ASM International Handbook Committee, 2009, Ch. Fundamentals of the Modeling of Microstructure and Texture Evolution, pp. 203–219.

[13] J. Rowlinson, Translation of J. D. van der Waals' "The thermodynamic theory of capillarity under the hypothesis of a continuous variation of density", Journal of statistical physics 20 (1979) 197–245.

[14] V. Ginzburg, L. Landau, Toward the superconductivity theory, Zhurnal Eksp. Yheoret. Physics 29 (1950) 1064–1082.

[15] J. Cahn, J. Hilliard, Free Energy of a Nonuniform System. I. Interfacial Free Energy, The Journal of Chemical Physics 28 (2) (1958) 258–267.

[16] Y. Ji, B. Ghaffari, M. Li, L.-Q. Chen, Phase-Field Modeling of θ' Precipitation Kinetics in W319 Alloys, in: P. Mason, C. Fisher, R. Glamm, M. Manuel, G. Schmitz, S. Amarendra K., A. Strachan (Eds.), Proceedings of the 4th World Congress on Integrated Computational Materials Engineering (ICME 2017), Springer International Publishing, Cham, 2017, pp. 293–304.

[17] Y. Zhang, J. Wang, Y. Yang, G. Yang, Y. Zhou, Phase-Field Simulation of the Elastic Effect on the Transformation Kinetics in Precipitation, Materials Transactions 49 (2008) 133–138.

[18] N. Zhou, D. Lv, H. Zhang, D. McAllister, F. Zhang, M. Mills, Y. Wang, Computer simulation of phase transformation and plastic deformation in

IN718 superalloy: Microstructural evolution during precipitation, Acta Materialia 65 (2015) 270–286.

[19] M. Volmer, A. Weber, Keimbildung in übersättigten Gebilden, Zeitschrift für Physikalische Chemie 119U (1926) 707–713.

[20] M. Becker, W. Döring, Kinetische Behandlung der Keimbildung in übersättigten Dämpfen, Annalen der Physik 24 (1935) 719–752.

[21] J. Frenkel, Statistical Theory of Condensation Phenomena, The Journal of Chemical Physics 7 (1939) 200–201.

[22] J. Frenkel, A General Theory of Heterophase Fluctuations and Pretransition Phenomena, The Journal of Chemical Physics 7 (1939) 538–547.

[23] Y. Zeldovich, On the theory of a new phase formation: Cavitation, Acta physicochimica USSR 18 (1943) 1–22.

[24] K. Russell, Phase transformations, American Society for Metals, 1968, Ch. Nucleation on Solids, pp. 219–268.

[25] R. Kampmann, R. Wagner, Decomposition of alloys: the early stages, Pergamon Press, 1984, Ch. Chapter Kinetics of precipitation in metastable binary alloys – theory and application to Cu–1.9 at% Ti and Ni–14 at% Al, pp. 91–103.

[26] C. Zener, Theory of Growth of Spherical Precipitates from Solid Solution, Journal of Applied Physics 20 (1949) 950–953.

[27] I. Lifshitz, V. Slyozov, The kinetics of precipitation from supersaturated solid solutions, Journal of Physics and Chemistry of Solids 19 (1961) 35–50.

[28] C. Wagner, Theorie der alterung von niederschlägen durch umlösen, Zeitschrift für Elektrochemie 65 (1961) 581–594.

[29] A. Deschamps, Y. Brechet, Influence of predeformation and agEing of an Al–Zn–Mg alloy—II. Modeling of precipitation kinetics and yield stress, Acta Materialia 47 (1998) 293–305.

[30] R. Kampmann, R. Wagner, Materials Science and Technology: a comprehensive treatment., John Wiley & Sons Inc., 1991, Ch. Homogeneous second phase precipitation, pp. 213–302.

[31] O. Myrh, O. Grong, Modelling of non-isothermal transformations in alloys containing a particle distribution, Acta Materialia 48 (2000) 1605–1615.

[32] D. den Ouden, F. Vermolen, L. Zhao, C. Vuik, J. Sietsma, Modelling of particle nucleation and growth in binary alloys under elastic deformation: An application to a Cu–0.95wt% Co alloy, Computational Materials Science 50 (8) (2011) 2397–2410.

[33] D. den Ouden, L. Zhao, C. Vuik, J. Sietsma, F. Vermolen, Modelling precipitate nucleation and growth with multiple precipitate species under isothermal conditions: Formulation and analysis, Computational Materials Science 79 (2013) 933–943.

[34] N. Kamp, A. Sullivan, R. Tomasi, J. Robson, Modelling Heterogeneous Precipitation in 7xxx Aluminium Alloys during Complex Processing, Materials Science Forum 519-521 (2006) 1435–1440.

[35] M. Dumont, A. Deschamps, Characterization and modelling of precipitate evolution in an Al–Zn–Mg alloy during non-isothermal heat treatments, Acta Materialia 51 (2003) 6077–6094.

[36] P. Maugis, M. Gouné, Kinetics of vanadium carbonitride precipitation in steel: A computer model, Acta Materialia 53.

[37] M. Perez, E. Courtois, D. Acevedo-Reyes, T. Epicier, P. Maugis, Precipitation of niobium carbonitrides in ferrite: chemical composition measurements and thermodynamic modelling, Philosophical Magazine Letters 87 (2007) 645–656.

[38] M. Perez, M. Dumont, D. Acevedo-Reyes, Implementation of classical nucleation and growth theories for precipitation, Acta Materialia 56 (2008) 2119–2132.

[39] A. Kolmogorov, Statistical theory of crystallization of metals, Izv. Akad. Nauk SSSR, Ser. Mat 1 (1937) 355–359.

[40] W. Johnson, R. Mehl, Reaction kinetics in processes of nucleation and growth, Transactions of the American Institute of Mining and Metallurgical Engineers 135 (1939) 416.

[41] K. Barmak, A commentary on: "reaction kinetics in processes of nucleation and growth", Metallurgical and Materials Transactions A 41 (11) (2010) 2711–2775.

[42] M. Avrami, Kinetics of Phase Change. I. General Theory, The Journal of Chemical Physics 7 (1939) 1103–1112.

[43] M. Avrami, Kinetics of Phase Change. II Transformation-Time Relations for Random Distribution of Nuclei, The Journal of Chemical Physics 8 (1940) 212.

[44] M. Avrami, Kinetics of Phase Change. III. Granulation, Phase Change, and Microstructure, The Journal of Chemical Physics 7 (1941) 177–184.

[45] J. S. Langer, A. J. Schwartz, Kinetics of nucleation in near-critical fluids, Physical Review A 21 (1980) 948–958.

[46] R. Kampmann, R. Wagner, Decomposition of alloys: the early stages., Pergamon Press, 1984, Ch. Kinetics of precipitation in metastable binary alloys – theory and application to Cu–1.9 at

[47] M. Perez, M. Dumont, D. Acevedo-Reyes, Corrigendum to "Implementation of classical nucleation and growth theories for precipitation" [Acta Materialia 56 (2008) 2119–2132], Acta Materialia 57 (2009) 1318.

[48] M. V. Smoluchowski, Drei vorträge über diffusion, brownsche molekularbewegung und koagulation von kolloidteilchen, Phys. Z 17 (1916) 557–571, 585–599.

[49] L. Ratke, Coarsening of liquid Al–Pb dispersions under reduced gravity conditions, Materials Science and Engineering: A 203 (1) (1995) 399–407.

[50] W. Ostwald, Studien über die bildung und umwandlung fester körper, Zeitschrift für physikalische Chemie 22 (1897) 289–330.

[51] F. Masoumi, M. Jahazi, D. Shahriari, J. Cormier, Coarsening and dissolution of γ' precipitates during solution treatment of AD730$^{\text{TM}}$ Ni-based superalloy: Mechanisms and kinetics models, Journal of Alloys and Compounds 658 (2016) 981–995.

[52] R. Cozar, G. Rigaut, A. Pineau, Durcissement par précipitation d'un alliage Fe - 30 % Ni - 9 % Ta, Scripta Metallurgica 3 (12) (1969) 883–886.

[53] W. Quist, R. Taggart, D. Polonis, The influence of iron and aluminum on the precipitation of metastable Ni_3Nb phases in the Ni-Nb system, Metallurgical Transactions 2 (3) (1971) 825–832.

[54] S. Floreen, G. Fuchs, W. Yang, The metallurgy of alloy 625, in: E. Loria (Ed.), Superalloys 718, 625, 706 and Various Derivatives, TMS (The Minerals, Metals & Materials Society), Warrendale, PA, 1994, pp. 13–37.

[55] R. Cozar, A. Pineau, Influence of the Co/Ni ratio on the γ' and γ'' precipitation in Fe-Ni-Co-Ta alloys, Metallurgical Transactions 5 (11) (1974) 2471–2472.

[56] H. Eiselstein, J. Gadbut, Matrix-stiffened alloy, US patent number 3,160,500 (December 1964).

[57] J. Radavich, A. Fort, Effects of Long-Time Exposure in Alloy 625 at 1200° F, 1400° F and 1600° F, in: E. Loria (Ed.), Superalloys 718, 625, and Various Derivatives, TMS (The Minerals, Metals & Materials Society), Warrendale, PA, 1994, pp. 635–647.

[58] M. Sundararaman, R. Kishore, P. Mukhopadhyay, Some aspects of the heterogeneous precipitation of the metastable γ'' phase in alloy 625, in:

E. Loria (Ed.), Superalloys 718, 625, 706 and Various Derivatives, TMS (The Minerals, Metals & Materials Society), Warrendale, PA, 1994, pp. 405–417.

[59] V. Shankar, K. B. S. Rao, S. Mannan, Microstructure and mechanical properties of Inconel® 625 superalloy, Journal of Nuclear Materials 288 (2) (2001) 222–232.

[60] H. Pai, M. Sundararaman, A comparison of the precipitation kinetics of γ'' particles in virgin and re-solutioned alloy 625, in: E. Loria (Ed.), Superalloys 718, 625, and Various Derivatives, TMS (The Minerals, Metals & Materials Society), Warrendale, PA, 2005, pp. 487–495.

[61] L. M. Suave, D. Bertheau, J. Cormier, P. Villechaise, A. Soula, Z. Hervier, J. Laigo, Impact of microstructural evolutions during thermal aging of alloy 625 on its monotonic mechanical properties, MATEC Web of conference 21 (2015) 21001.

[62] A. Devaux, L. Nazé, R. Molins, A. Pineau, A. Organista, J. Guédou, J. Uginet, P. Héritier, Gamma double prime precipitation kinetic in Alloy 718, Materials Science and Engineering 486 (2008) 117–122.

[63] J. W. Gibbs, On the Equilibrium of Heterogeneous Substances, Transactions of the Connecticut Academy of Arts and Sciences 3 (1875) 108–248.

[64] J. W. Gibbs, On the Equilibrium of Heterogeneous Substances, Transactions of the Connecticut Academy of Arts and Sciences 3 (1875) 343–524.

[65] J. Thompson, Theoretical considerations on the effect of pressure in lowering the freezing point of water, Transactions of the Royal Society of Edinburgh 16 (1849) 575–580.

[66] J. Thompson, On crystallization and liquefaction, as influenced by stresses tending to changes of form of crystals, Proceedings of the Royal Society of London 11 (1862) 473–481.

[67] J. Thompson, On the equilibrium at vapor at a curved surface of a liquid, Philosophical Magazine 42 (1871) 448–452.

[68] M. Perez, Approche multi-échelle de la précipitation, Tech. rep., École doctorale matériaux de Lyon, université de Lyon, mémoire d'habilitation à diriger des recherches (2007).
URL https://tel.archives-ouvertes.fr/tel-00511311/document

[69] A. Devaux, B. Picqué, M. Gervais, E. Georges, T. Poulain, P. Héritier, AD730$^{\mathrm{TM}}$ - a new nickel-based superalloy for high temperature engine rotative parts, in: E. Huron, R. Reed, M. Hardy, M. Mills, R. Montero, P. Portella, J. Telesman (Eds.), 12$^{\mathrm{th}}$ International Symposium on Superalloys, TMS (The Minerals, Metals & Materials Society), 2012, pp. 911–919.

[70] F. Masoumi, D. Shahriari, M. Jahazi, J. Cormier, A. Devaux, Kinetics and mechanisms of γ' reprecipitation in a ni-based superalloy, Scientific Reports 6 (2016) 28650.

[71] R. Radis, M. Schaffer, M. Albu, G. Kothleitner, P. Pölt, E. Kozeschnik, Multimodal size distributions of γ' precipitates during continuous cooling of UDIMET 720 Li, Acta Materialia 57 (19) (2009) 5739–5747. doi:https://doi.org/10.1016/j.actamat.2009.08.002.
URL http://www.sciencedirect.com/science/article/pii/S1359645409005035

[72] A. Singh, S. Nag, J. Hwang, G. Viswanathan, J. Tiley, R. Srinivasan, H. Fraser, R. Banerjee, Influence of cooling rate on the development of multiple generations of γ' precipitates in a commercial nickel base superalloy, Materials Characterization 62 (9) (2011) 878–886. doi:https://doi.org/10.1016/j.matchar.2011.06.002.
URL http://www.sciencedirect.com/science/article/pii/S1044580311001422

[73] A. Singh, S. Nag, S. Chattopadhyay, Y. Ren, J. Tiley, G. Viswanathan, H. Fraser, R. Banerjee, Mechanisms related to different generations of γ' precipitation during continuous cooling of a

nickel base superalloy, Acta Materialia 61 (1) (2013) 280–293. doi:https://doi.org/10.1016/j.actamat.2012.09.058.
URL http://www.sciencedirect.com/science/article/pii/S135964541200691X

[74] F. Schulz, H. Li, H. Kitaguchi, D. Child, S. Williams, P. Bowen, Influence of tertiary gamma prime (γ') size evolution on dwell fatigue crack growth behavior in cg rr1000, Metallurgical and Materials Transactions A 49 (2018) 3874–3884. doi:10.1007/s11661-018-4779-9.

[75] S. Semiatin, D. Mahaffey, N. Levkulich, O. Senkov, J. Tiley, The effect of cooling rate on high-temperature precipitation in a powder-metallurgy, gamma/gamma-prime nickel-base superalloy, Metallurgical and Materials Transactions A 49 (12) (2018) 6265–6276.
URL https://doi.org/10.1007/s11661-018-4896-5

[76] S. Saltykov, The determination of the size distribution of particles in an opaque material from a measurement of the size distribution of their sections, in: H. Elias (Ed.), Stereology, Springer Berlin Heidelberg, Berlin, Heidelberg, 1967, pp. 163–173.

[77] D. Scott, On optimal and data-based histograms, Biometrika 66 (1979) 605–610.

[78] M. Sundararaman, L. Kumar, G. E. Prasad, P. Mukhopadhyay, S. Banerjee, Precipitation of an intermetallic phase with Pt_2Mo-type structure in alloy 625, Metallurgical and Materials Transactions 30 (1) (1999) 41–52.

[79] L. M. Suave, J. Cormier, P. Villechaise, A. Soula, Z. Hervier, D. Bertheau, J. Laigo, Microstructural evolutions during thermal aging of alloy 625: Impact of temperature and forming process, Metallurgical and Materials Transactions 45 (2014) 2963–2982.

[80] P. Mukherjee, A. Sarkar, P. Barat, Lattice Misfit Measurement in Inconel® 625 by X-Ray Diffraction Technique, International Journal of Modern Physics B 22 (2008) 3977–3985.

[81] H. Yasuda, T. Takasugi, M. Koiwa, Elasticity of Ni-based L12-type intermetallic compounds, Acta Metallurgica et Materialia 40 (1992) 381–287.

[82] J. Chenot, P. Bouchard, L. Fourment, P. Lasne, E. Roux, Optimization of metal forming processes for improving final mechanical strength, in: E. Oñate, D. Owen, D. Peric, B. Suárez (Eds.), XI International Conference on Computational Plasticity. Fundamentals and Applications, 2011.

[83] A. Seret, C. Moussa, M. Bernacki, N. Bozzolo, On the Coupling between Recrystallization and Precipitation Following Hot Deformation in a γ-γ' Nickel-Based Superalloy, Metallurgical and Materials Transactions A 49 (2018) 4199–4213.

[84] A. Seret, Influence de la mise en forme sur les cinétiques de précipitation durcissante dans les superalliages base nickel Inconel 625 et AD730TM, Ph.D. thesis, PSL Research University, Mines ParisTech (2019).

[85] E. Hornbogen, The role of strain energy during precipitation of copper and gold from alpha iron, Acta Metallurgica 10 (5) (1962) 525–533.

[86] J. Cahn, Nucleation on dislocations, Acta Metallurgica 5 (1957) 169–172.

Appendix A. Calculation of the agglomerations number

In this appendix is detailed the calculation of $\mathcal{N}_V^{\text{agg}}$ the number of agglomerations by contact between growing precipitates during a time-step, leading to equation 1. The probability of an event $\mathcal{E}$ is denoted as $\mathbb{P}(\mathcal{E})$. Hereafter, positions and distances refer to the centers of precipitates. Since precipitates centers are placed randomly and independently, $\mathcal{N}_V^{\text{agg}}$ is written as the product of two factors. The first factor is the probability $\mathbb{P}(\mathcal{C})$ that a precipitate touches another when growing during the time-step, and is identical for all precipitates. The second factor is the number $\frac{N_V}{2}$ of possible agglomerations where the factor $\frac{1}{2}$ takes into account the fact that two precipitates touching each other account for two contacts but only one agglomeration.

$$\mathcal{N}_V^{\text{agg}} = \mathbb{P}(\mathcal{C}) \cdot \frac{N_V}{2}. \tag{A.1}$$

The goal is then to calculate $\mathbb{P}(\mathcal{C})$. To that, consider the beginning of the time-step and one precipitate of radius $\overline{r}$, named *central precipitate* and used for the calculation of $\mathbb{P}(\mathcal{C})$. Consider the sphere of radius R and volume V concentric with the central precipitate, where R is chosen big enough such that $N_V \cdot V$ is an integer. Then inside this sphere and around the central precipitate, $N-1$ other *neighbouring precipitates* of radius $\overline{r}$ are inserted, where $N = N_V \cdot V$. Any superimposition of precipitates is forbidden (especially with the central precipitate); this implies that neighbouring precipitates are distant from the central one by at least $\underbrace{\overline{r}}_{\substack{\text{central}\\ \text{precipitate}}} + \underbrace{\overline{r}}_{\substack{\text{neighbouring}\\ \text{precipitate}}} = 2 \cdot \overline{r}$. Moreover, neighbouring precipitates are inserted such that at the end of the time-step, they stay entirely included inside the sphere of radius R, which implies that they are distant from the central precipitate by at most $R - \left(\overline{r} + \dot{\overline{r}} \cdot \Delta t\right)$. These two previous conditions imply that centers of neighbouring precipitates are all in the spherical shell $\mathtt{S}_{2\cdot\overline{r}}^{R-\left(\overline{r}+\dot{\overline{r}}\cdot\Delta t\right)}$ of internal radius $2\cdot\overline{r}$ and external radius $R-\left(\overline{r}+\dot{\overline{r}}\cdot\Delta t\right)$. The configuration at the beginning of the time-step is then indeed N_V precipitates per unit volume of material and whose mean precipitate radius is $\overline{r}$, illustrated in figure A.8 where the radius $\overline{r}+\dot{\overline{r}}\cdot\Delta t$ at the end of the time-step is also shown,

semi-transparent. To calculate $\mathbb{P}(\mathcal{C})$ consider the event $\overline{\mathcal{C}}$ complementary of $\mathcal{C}$, that is the *non-occurence* of contact between the central precipitate and any neighbouring precipitate. Then:

$$\mathbb{P}(\mathcal{C}) = 1 - \mathbb{P}\left(\overline{\mathcal{C}}\right). \tag{A.2}$$

The event $\overline{\mathcal{C}}$ is practical from the calculatory point of view, because it consists in the intersection of several independent events. These events are of the type "the central precipitate does *not* touch the precipitate p" where p refers a neighbouring precipitate. More precisely, p can be the neighbouring precipitate number 1, 2, ..., up to $N-1$. Moreover, possible precipitates referred to by p are placed randomly, so these events are independent. Thus $\mathbb{P}\left(\overline{\mathcal{C}}\right)$ is the product of the probabilities of all these events. The probability of *not* touching the neighbouring precipitate number i is denoted as $\mathbb{P}\left(\overline{\overline{\mathcal{C}}}_{1\text{ prec}}\right)$, omitting the subscript i because all neighbouring precipitates are placed according to the *same* random law, so this probability does not depend on i. Then it comes:

$$\mathbb{P}\left(\overline{\mathcal{C}}\right) = \left(\mathbb{P}\left(\overline{\overline{\mathcal{C}}}_{1\text{ prec}}\right)\right)^{N-1}. \tag{A.3}$$

To calculate $\mathbb{P}\left(\overline{\overline{\mathcal{C}}}_{1\text{ prec}}\right)$, a key element is the distance between the central precipitate and a neighbouring precipitate. Indeed, the non-occurence of contact means that this distance is greater than $\underbrace{\overline{r} + \overline{\dot{r}} \cdot \Delta t}_{\substack{\text{radius of} \\ \text{central precipitate} \\ \text{at the end of the time-step}}} + \underbrace{\overline{r} + \overline{\dot{r}} \cdot \Delta t}_{\substack{\text{radius of} \\ \text{neighbouring precipitate} \\ \text{at the end of the time-step}}}$. This means that the neighbouring precipitate has its center in the spherical shell $\mathtt{S}_{2\cdot\left(\overline{r}+\overline{\dot{r}}\cdot\Delta t\right)}^{R-\left(\overline{r}+\overline{\dot{r}}\cdot\Delta t\right)}$ of internal radius $2\left(\overline{r} + \overline{\dot{r}} \cdot \Delta t\right)$ and external radius $R-\left(\overline{r} + \overline{\dot{r}} \cdot \Delta t\right)$. This is always true if $\overline{\dot{r}} \leq 0$. On the calculation side, $\mathbb{P}\left(\overline{\overline{\mathcal{C}}}_{1\text{ prec}}\right) = 1$, so $\mathbb{P}\left(\overline{\mathcal{C}}\right) = 1$ thus $\mathbb{P}(\mathcal{C}) = 0$, hence $\mathcal{N}_V^{\text{agg}} = 0$. On the physical side, if $\overline{\dot{r}} < 0$ precipitates are globally shrinking, which suggests that agglomeration by contact is negligible, which is consistent with the calculation result $\mathcal{N}_V^{\text{agg}} = 0$. If $\overline{\dot{r}} > 0$, then $\mathbb{P}\left(\overline{\overline{\mathcal{C}}}_{1\text{ prec}}\right)$ equals the ratio between the volume of the spherical shell $\mathtt{S}_{2\cdot\left(\overline{r}+\overline{\dot{r}}\cdot\Delta t\right)}^{R-\left(\overline{r}+\overline{\dot{r}}\cdot\Delta t\right)}$ (where must lie the neighbouring precipitate to avoid the contact with the central one) and the one of the spherical shell $\mathtt{S}_{2\cdot\overline{r}}^{R-\left(\overline{r}+\overline{\dot{r}}\cdot\Delta t\right)}$ (where lies

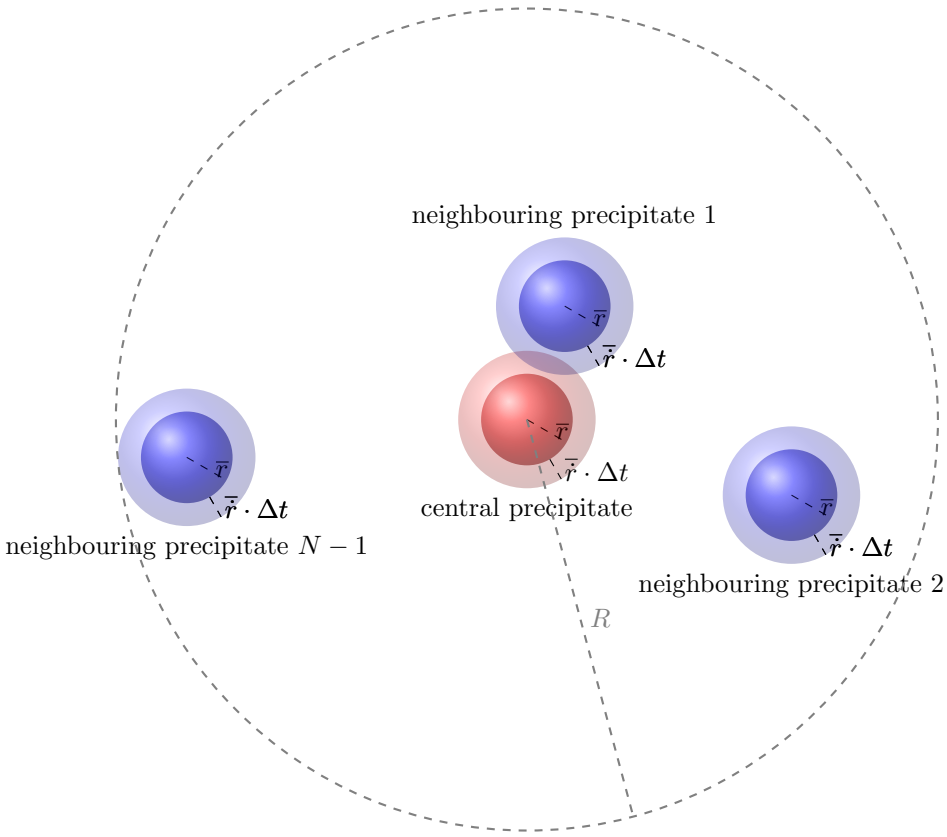

Figure A.8: Geometrical model considered to assess the number of agglomerations per unit volume during a time-step $\mathcal{N}_V^{\text{agg}}$. Positioning of the $N-1$ neighbouring precipitates (blue) around the central precipitate (red) in the sphere of radius R and volume V. The radius R is chosen such that $N_V \cdot V$ $(= N)$ is an integer. Precipitates are placed such that there is no superposition *at the start of the time-step* and such that neighbouring precipitates stay entirely inside the sphere (including at the end of the time-step, where the limit case is illustrated by the neighbouring precipitate $N-1$ on the left) the sphere of radius R. The semi-transparent spherical shell of thickness $\dot{\bar{r}} \cdot \Delta t$ represents the growth of precipitates during the time-step Δt with the radius time derivative $\dot{\bar{r}}$.

the neighbouring precipitates when it is inserted in the sphere of radius R). To merge both cases ($\overline{\dot{r}} \leq 0$ et $\overline{\dot{r}} > 0$) in a unified mathematical formulation, the positive part of the mean of the time derivative of radii, also denoted as $\overline{\dot{r}}_+$, is defined by $\overline{\dot{r}}_+ = \max\left\{\overline{\dot{r}}, 0\right\}$. Thus the probability $\mathbb{P}\left(\overline{\overline{\mathcal{C}}}_{1 \text{ prec}}\right)$ is:

$$\mathbb{P}\left(\overline{\overline{\mathcal{C}}}_{1 \text{ prec}}\right) = \frac{\frac{4}{3}\cdot\pi\cdot\left(R-\left(\overline{r}+\overline{\dot{r}}_+\cdot\Delta t\right)\right)^3 - \frac{4}{3}\cdot\pi\cdot\left(2\cdot\left(\overline{r}+\overline{\dot{r}}_+\cdot\Delta t\right)\right)^3}{\frac{4}{3}\cdot\pi\cdot\left(R-\left(\overline{r}+\overline{\dot{r}}_+\cdot\Delta t\right)\right)^3 - \frac{4}{3}\cdot\pi\cdot\left(2\cdot\overline{r}\right)^3} \tag{A.4}$$

$$= \frac{\left(R-\left(\overline{r}+\overline{\dot{r}}_+\cdot\Delta t\right)\right)^3 - \left(2\cdot\left(\overline{r}+\overline{\dot{r}}_+\cdot\Delta t\right)\right)^3}{\left(R-\left(\overline{r}+\overline{\dot{r}}_+\cdot\Delta t\right)\right)^3 - \left(2\cdot\overline{r}\right)^3}. \tag{A.5}$$

Thus

$$\mathbb{P}\left(\overline{\mathcal{C}}\right) = \left(\frac{\left(R-\left(\overline{r}+\overline{\dot{r}}_+\cdot\Delta t\right)\right)^3 - \left(2\cdot\left(\overline{r}+\overline{\dot{r}}_+\cdot\Delta t\right)\right)^3}{\left(R-\left(\overline{r}+\overline{\dot{r}}_+\cdot\Delta t\right)\right)^3 - \left(2\cdot\overline{r}\right)^3}\right)^{N-1}. \tag{A.6}$$

However, until now a finite material volume (V, the sphere of radius R) has been considered. To quantify averaged phenomena, consider an infinite volume of material. To that, let V tend towards infinity (by letting R tend towards infinity) while keeping N_V constant. Indeed, N_V, the number of precipitates per unit volume of material at the beginning of the time-step, is independent of the material volume. Let then rewrite the right member of equation A.6 to obtain the development for $V \to \infty$ *i.e.* for $R \to \infty$:

$$\mathbb{P}\left(\overline{\mathcal{C}}\right) = \left(\frac{\left(R-\left(\overline{r}+\overline{\dot{r}}_+\cdot\Delta t\right)\right)^3 - \left(2\cdot\left(\overline{r}+\overline{\dot{r}}_+\cdot\Delta t\right)\right)^3}{\left(R-\left(\overline{r}+\overline{\dot{r}}_+\cdot\Delta t\right)\right)^3 - \left(2\cdot\overline{r}\right)^3}\right)^{N-1} \tag{A.7}$$

$$= \exp\left((N-1)\cdot\ln\left(\frac{\left(R-\left(\overline{r}+\overline{\dot{r}}_+\cdot\Delta t\right)\right)^3 - \left(2\cdot\left(\overline{r}+\overline{\dot{r}}_+\cdot\Delta t\right)\right)^3}{\left(R-\left(\overline{r}+\overline{\dot{r}}_+\cdot\Delta t\right)\right)^3 - \left(2\cdot\overline{r}\right)^3}\right)\right) \tag{A.8}$$

$$= \exp\left((N-1)\cdot\ln\left(1-\epsilon\right)\right), \tag{A.9}$$

posing

$$\epsilon = \frac{\left(2\cdot\left(\overline{r}+\overline{\dot{r}}_+\cdot\Delta t\right)\right)^3 - \left(2\cdot\overline{r}\right)^3}{\left(R-\left(\overline{r}+\overline{\dot{r}}_+\cdot\Delta t\right)\right)^3 - \left(2\cdot\overline{r}\right)^3}. \tag{A.10}$$

When considering the Taylor expansion at the first order of the neperian logarithm, since $R \to \infty$ implies that $\epsilon \to 0$:

$$\mathbb{P}\left(\overline{\mathcal{C}}\right) =_{R\to\infty} \exp\left(\left(N_V \cdot V - 1\right) \cdot \left(-\frac{\left(2 \cdot \left(\overline{r} + \dot{\overline{r}}_+ \cdot \Delta t\right)\right)^3 - \left(2 \cdot \overline{r}\right)^3}{\left(R - \left(\overline{r} + \dot{\overline{r}}_+ \cdot \Delta t\right)\right)^3 - \left(2 \cdot \overline{r}\right)^3} + \mathcal{O}\left(\frac{1}{R^6}\right)\right)\right) \tag{A.11}$$

$$=_{R\to\infty} \exp\left(\left(N_V \cdot \frac{4}{3} \cdot \pi \cdot R^3 - 1\right) \cdot \left(-\frac{\left(2 \cdot \left(\overline{r} + \dot{\overline{r}}_+ \cdot \Delta t\right)\right)^3 - \left(2 \cdot \overline{r}\right)^3}{\left(R - \left(\overline{r} + \dot{\overline{r}}_+ \cdot \Delta t\right)\right)^3 - \left(2 \cdot \overline{r}\right)^3} + \mathcal{O}\left(\frac{1}{R^6}\right)\right)\right) \tag{A.12}$$

$$=_{R\to\infty} \exp\left(-N_V \cdot \frac{4}{3} \cdot \pi \cdot \frac{R^3}{\left(R - \left(\overline{r} + \dot{\overline{r}}_+ \cdot \Delta t\right)\right)^3 - \left(2 \cdot \overline{r}\right)^3} \cdot \left(\left(2 \cdot \left(\overline{r} + \dot{\overline{r}}_+ \cdot \Delta t\right)\right)^3 - \left(2 \cdot \overline{r}\right)^3\right) + \mathcal{O}\left(\frac{1}{R^3}\right)\right) \tag{A.13}$$

$$\to_{R\to\infty} \exp\left(-N_V \cdot \frac{4}{3} \cdot \pi \cdot \left(\left(2 \cdot \left(\overline{r} + \dot{\overline{r}}_+ \cdot \Delta t\right)\right)^3 - \left(2 \cdot \overline{r}\right)^3\right)\right) \tag{A.14}$$

$$= \quad \exp\left(-\mathcal{N}_*^{\text{agg}}\right) \tag{A.15}$$

where

$$\mathcal{N}_*^{\text{agg}} = \frac{4}{3} \cdot \pi \cdot N_V \cdot \left(\left(2 \cdot \left(\overline{r} + \dot{\overline{r}}_+ \cdot \Delta t\right)\right)^3 - \left(2 \cdot \overline{r}\right)^3\right). \tag{A.16}$$

Inserting notably equations A.16 and A.15 in equation A.2 supplies the number $\mathcal{N}_V^{\text{agg}}$ of agglomerations per unit volume during the time-step (equation 1).

Appendix B. Validation by full field simulations of the calculation of the agglomeration number per unit volume

In this appendix, the calculation of the agglomerations number during a time-step developed in Appendix A is checked using full field simulations. A set of 200000 spheres of radius $\overline{r}$ have been inserted in a cube representing the material domain (matrix $\cup$ precipitates). Their centers are placed randomly but (1) avoiding any superimposition and (2) guaranteeing that by increasing their radii by $\dot{\overline{r}} \cdot \Delta t$ (representing the radius at the end of the time-step) spheres are still entirely inside the cube. The cube edge length is calculated such that the number of spheres divided by the cube volume equals N_V. These spheres represent the precipitates at the beginning of a time-step and are illustrated

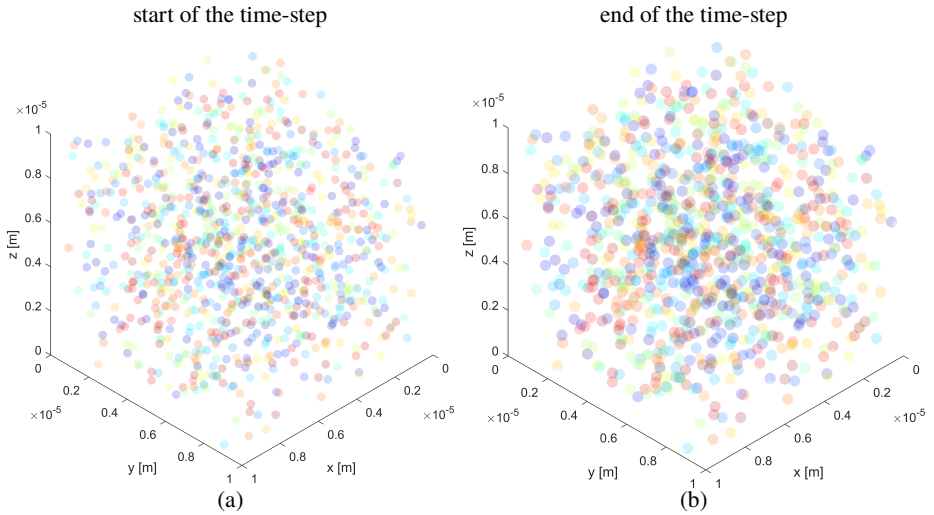

Figure B.9: Spheres places randomly inside a cube to check the validity of the mean field calculation of the number of agglomerations $\mathcal{N}_V^{\text{agg}}$ during a time-step (appendix A) by a full field simulation. Spheres represent precipitates at (a) the start of the time-step and (b) the end of the time-step. Their radius is $\overline{r}$ and $\overline{r} + \dot{\overline{r}} \cdot \Delta t$ at the start and the end of the time-step, respectively, and their number divided by the cube volume is N_V. Spheres are placed at the start of the time-step without superposition, and such that at the end of the time-step they are still fully included inside the cube. Values of $\overline{r}$, N_V and $\dot{\overline{r}}$ are the ones for the simulation 15 (defined in the table B.3). However, in the simulation used for this figure, 1000 spheres only have been placed for the sake of readability; in actual full field simulations (table B.3), 200000 spheres have been placed.

for one simulation in figure B.9. To simulate the size evolution of precipitates during a time-step Δt, a time derivative of the radius common to all spheres is considered. Using the distances between sphere centers and their (common) radius $\overline{r} + \dot{\overline{r}} \cdot \Delta t$ at the end of the time-step, it is determined for each spheres whether it met another one during the time-step. For each sphere, the boolean 1 is assigned if it meets another sphere during the time-step and 0 otherwise. The sum of these booleans on all spheres, divided by the cube volume, is the encounter number per unit volume. This number corresponds to $\mathbb{P}(\mathcal{C}) \cdot N_V$ in equation A.1. The agglomeration number per unit volume $\mathcal{N}_V^{\text{agg}}$ is then calculated by taking the half (equation A.1). To compare mean field and full field approaches, the agglomeration number calculated by the mean field approach is also considered. To that, $\mathcal{N}_V^{\text{agg}}$ the agglomeration number per unit volume is calculated by the mean field method (equations A.1, A.2, A.15 and A.16) and is multiplied by the cube volume. Different simulations have been performed by taking 3 different values for each one of the 3 parameters (mean radius $\overline{r}$, precipitates number per unit volume N_V, mean radius time derivative $\dot{\overline{r}}$) which could influence results, supplying 27 simulations. Chosen values aim at representing realistic values for experimental precipitate populations. The three values are separated by factors of 4. Adding lower values would be useless since no agglomeration occur for low enough mean radius, precipitate number per unit volume or mean radius time derivative. Conversely, adding higher values would be again useless since all precipitates would then meet. The results of full field simulations and mean field calculations using equations A.1, A.2, A.15 and A.16) are summarized in table B.3 and illustrated in figure B.10. Agglomeration numbers calculated by the mean field calculation and obtained from the full field simulations (table B.3 and figure B.10) are close enough to support the mean field calculation developed in appendix A.

simulation id	$\overline{r}$ [nm]	N_V [μm^{-3}]	$\dot{\overline{r}}$ [$nm\,s^{-1}$]	agglomerations number	
				mean field	full field
1	10	0.25	10	5.9	6
2	40	0.25	10	51	37
3	160	0.25	10	680	714
4	10	1	10	23	25
5	40	1	10	204	216
6	160	1	10	2701	2746
7	10	4	10	94	79
8	40	4	10	814	802.5
9	160	4	10	10373	11821
10	10	0.25	40	104	93
11	40	0.25	40	375	381
12	160	0.25	40	3218	3277.5
13	10	1	40	415	434
14	40	1	40	1490	1459
15	160	1	40	12263	12682
16	10	4	40	1648	1697
17	40	4	40	5808	5809.5
18	160	4	40	40743	45968
19	10	0.25	160	4032	4034
20	40	0.25	160	6432	6482
21	160	0.25	160	21353	21540.5
22	10	1	160	15177	15316.5
23	40	1	160	23351	23344.5
24	160	1	160	61742	63673
25	10	4	160	48233	48022.5
26	40	4	160	65484	65756.5
27	160	4	160	97858	99052

Table B.3: Values used for the number of precipitates per unit volume N_V, mean radius $\overline{r}$ and mean radius time derivative $\dot{\overline{r}}$, and results in terms of agglomerations number during the time-step $\Delta t = 1\,s$ for mean field simulations (equations A.1, A.2, A.15 and A.16) and full field simulations (200 000 spheres placed without superposition inside a cube).

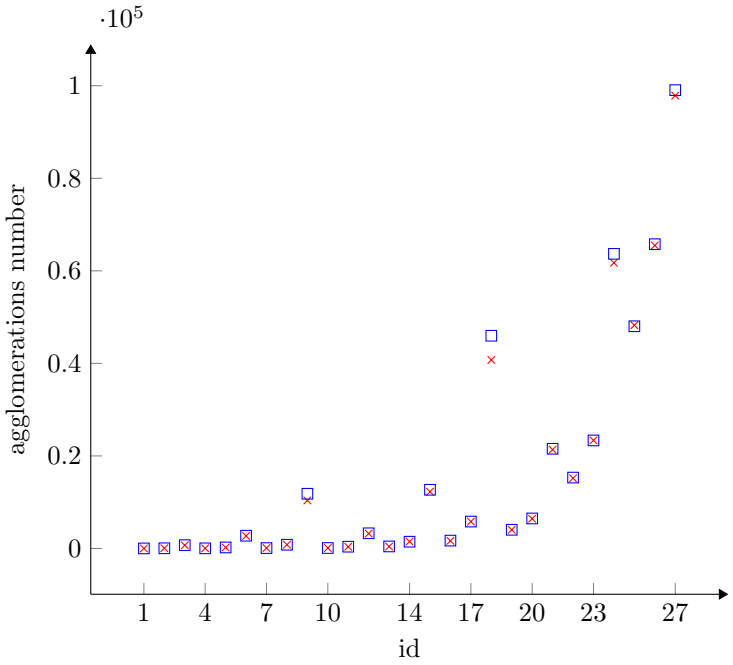

Figure B.10: Results (values in table B.3) in terms of agglomerations number during the time-step $\Delta t = 1\,\mathrm{s}$ for mean field calculations (red cross) (equations A.1, A.2, A.15 and A.16) and full field simulations (blue squares) (200 000 spheres placed without superposition inside a cube).

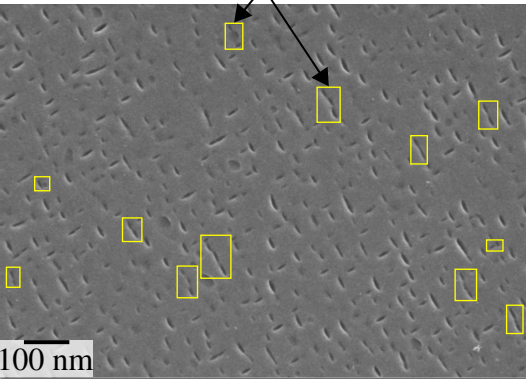

mean field precipitation model

classical approach
agglomeration not considered

start of time-step
precipitates
population

- nucleation
- size evolution

end of time-step
precipitates
population

number of agglomerations

end of time-step
precipitates
population

equivalent agglomeration model (EAM)